Prognostic Equation for Radar Radial Velocity Derived by Considering Atmospheric Refraction and Earth Curvature

QIN XU

NOAA/National Severe Storms Laboratory, Norman, Oklahoma

LI WEI

Cooperative Institute for Mesoscale Meteorological Studies, University of Oklahoma, Norman, Oklahoma

(Manuscript received 7 January 2013, in final form 31 May 2013)

ABSTRACT

The prognostic equation for the radial velocity field observed with a Doppler radar is derived to include the effects of atmospheric refraction and earth curvature on radar-beam height and slope angle. The derived equation, called the radial velocity equation, contains a high-order small term that can be truncated. The truncated radial velocity equation is shown to be much more accurate than its counterpart radial velocity equation derived without considering the effects of atmospheric refraction and earth curvature. The truncated equation has the same concise form as its counterpart radial velocity equation but remains to be sufficiently accurate as a useful dynamic constraint for radar wind analysis and assimilation (in normal situations) even up to the farthest 300-km radial range of operational Weather Surveillance Radar-1988 Doppler (WSR-88D) scans where its counterpart radial velocity equation becomes erroneous.

1. Introduction

The prognostic equation for radial velocity scanned from a Doppler radar, called the radial velocity equation, has been used in various simplified forms as a dynamic constraint for analyzing and assimilating radial velocity observations in space and time dimensions (Xu et al. 1994, 1995, 2001a,b; Xu and Qiu 1995; Qiu and Xu 1996). As the radial velocity observations used in these previous studies were confined in near-radar ranges (<20 km), the effects of atmospheric refraction and earth curvature on the radar-beam height and slope angle (relative to the earth surface below the measurement point) were neglected in the previously derived simple forms of the radial velocity equation. For operational Weather Surveillance Radar-1988 Doppler (WSR-88D) scans, the maximum radial range for radial velocity measurements has been extended recently to nearly 300 km. As the radial range increases to 300 km, the WSR-88D beam is about 5 km wide and the lowest beam center is above 7 km. In this case, the radial velocity measurements may become not useful for detecting mesocyclones (that can produce tornadoes) and related applications, but they are still useful for mesoscale data assimilation. For the operational North American Mesoscale Forecast System (NAM), the horizontal resolution is 12 km, so operational radar observations, even out to 300-km radial range, still have excessive horizontal resolutions with respect to NAM and therefore should be compressed into fewer superobservations (after quality control) to reduce their resolution redundancy (Xu 2011; Xu and Wei 2011) and then all assimilated into NAM.

To assimilate full volumes of operational radar data, it is necessary to properly consider the effects of atmospheric refraction and earth curvature on the radar-beam height and slope angle. According to Ge et al. (2010), neglecting these effects, especially the earth curvature effect, can cause significant and increasingly large errors in assimilated storm winds as the distance between the storm center and radar location increases to 60 km and beyond. The above effects have been considered in the 3.5-dimensional variational method (3.5DVar) (Gu et al. 2001; Zhao et al. 2006, 2008; Xu et al. 2010) and other radar data assimilation method (Gao et al. 2006, 2008) as well as the widely used Weather Research and Forecasting Model–Data Assimilation

Corresponding author address: Dr. Qin Xu, NSSL, 120 David L. Boren Blvd., Norman, OK 73072-7326.
E-mail: qin.xu@noaa.gov

DOI: 10.1175/JAS-D-13-011.1

Research Testbed (WRF-DART) radar data assimilation package (A. Caya and D. Dowell 2013, personal communication). The radial velocity equation in the 3.5DVar, however, was not derived rigorously to include the effects of atmospheric refraction and earth curvature and it also neglected the perturbation pressure and buoyancy terms. This paper aims to derive the radial velocity equation by considering the above effects and analyze the accuracy of the derived equation. The next section reviews the commonly used equivalent earth model for radar ray path. Section 3 derives the radial velocity equation using the equivalent earth model. Section 4 truncates the derived equation into a concise form and examines the accuracy of the truncated radial velocity equation in comparison with its counterpart equation derived without considering the effects of atmospheric refraction and earth curvature. Conclusions follow in section 5.

2. Review of equivalent earth model

The radial velocity observed by radar is related to the vector velocity $\mathbf{v} + w_T\mathbf{k}$ by

$$\upsilon_r^{\text{ob}} = \upsilon_r + \upsilon_{rT} \equiv (\mathbf{v} + w_T\mathbf{k})^{\text{T}}\mathbf{c} = u\cos\theta\sin\phi + \upsilon\cos\theta\cos\phi + (w + w_T)\sin\theta, \quad (2.1)$$

where $\upsilon_r \equiv \mathbf{v}^{\text{T}}\mathbf{c}$; $\upsilon_{rT} \equiv w_T\mathbf{k}^{\text{T}}\mathbf{c}$; superscript T denotes the transpose; $\mathbf{v} \equiv (u, \upsilon, w)^{\text{T}}$ is the vector velocity of air; $w_T\,(<0)$ is the terminal velocity of hydrometeors; $\mathbf{k}$ is the upward unit vector; $\mathbf{c} \equiv (\cos\theta\sin\phi, \cos\theta\cos\phi, \sin\theta)^{\text{T}}$ is the unit vector composed of the three directional cosines along the (curved) radar beam at the measurement point in the local Cartesian coordinate system, denoted by (x, y, z), centered at the radar; ϕ is the azimuthal angle (positive for clockwise rotation from the y coordinate pointing to the north); and θ is the radar-beam slope angle with respect to the curved earth surface immediately below the measurement point. Because of the atmospheric refraction and earth curvature, the radar beam is curved (usually concave upward relative to a flattened earth surface) as shown in Fig. 1, and

$$\theta = \theta_e + \psi_e, \quad (2.2)$$

where θ_e is the beam elevation angle at the radar, and ψ_e can be expressed as a function of (θ_e, r) in the equivalent earth model reviewed below [also see sections 2.2.3.1 and 9.3.1 of Doviak and Zrnic (2006), and note that the above θ is equivalent to θ_e' in their (9.9)], where r is the length of the curved beam (ray path) from the radar to the measurement point.

In the equivalent earth model, the refractivity index n is assumed to be horizontally uniform with a constant vertical gradient, typically around $dn/dz \approx -1/(4a)$ in the lower troposphere, so all low-elevation radar beams have about the same constant curvature and can be mapped into straight beams (with their radius of curvature "inflated" to infinity) by "inflating" the earth radius a to the effective radius $a_e = a/(1 + a dn/dz) \approx 4a/3$ [see (2.27) of Doviak and Zrnic (2006) or section 3 of Heymsfield et al. (1983)]. Approximately, to the first-order accuracy measured by $O(\psi_e)$ $[<O(r/a_e) \ll 1]$, each mapped straight beam preserves the length r of the originally curved beam and its height above the spherical equivalent earth of radius a_e preserves the height z of the originally curved beam above the curved earth surface. In the spherical coordinate system of the equivalent earth model (see Fig. 2), $R = a_e + z$ is the radial coordinate of the measurement point, $s = a_e\psi_e$ is the great-circle arc distance between the radar and the point immediately underneath the measurement point on the spherical surface of the equivalent earth, and ψ_e is the angle subtended by the two radii at the radar and measurement points. The related geometry is shown in Fig. 2. Applying the cosine law to the OB side and the sine law to the vertexes O and A of the triangle OAB in Fig. 2 gives

$$R^2 = r^2 + a_e^2 - 2ra_e\cos(\pi/2 + \theta_e) = r^2 + a_e^2 + 2ra_e\sin\theta_e \quad \text{and} \quad (2.3)$$

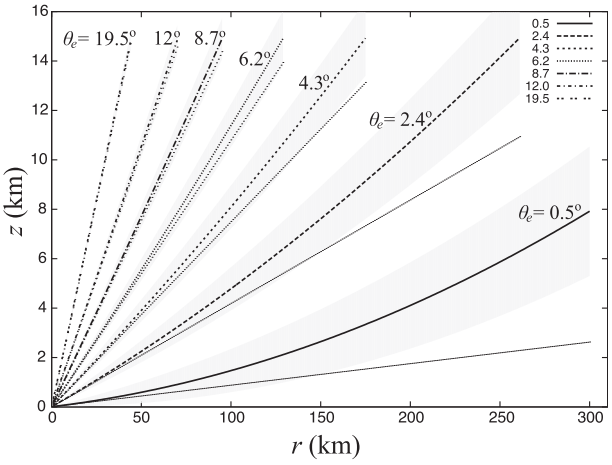

FIG. 1. Radar-beam height z [computed by (2.7) with $a_e = 4a/3$ in the equivalent earth model] plotted by dark curves as functions of the length of ray path r, for seven elevation angles (i.e., $\theta_e = 0.5°$, 2.4°, 4.3°, 6.2°, 8.7°, 12°, and 19.5° selected from the 14 elevation angles of $\theta_e = 0.5°$, 1.45°, 2.4°, 3.35°, 4.3°, 5.25°, 6.2°, 7.5°, 8.7°, 10°, 12°, 14°, 16.7°, and 19.5° in volume coverage patterns 11 and 211 used by the operational WSR-88Ds to scan thunderstorms). The shaded band around each dark curve shows the beam thickness (within $\theta_e \pm 0.5°$ for each θ_e). The thin dotted straight line associated with each dark curve is the beam height computed by $z = r\sin\theta_e$ in the flat earth model.

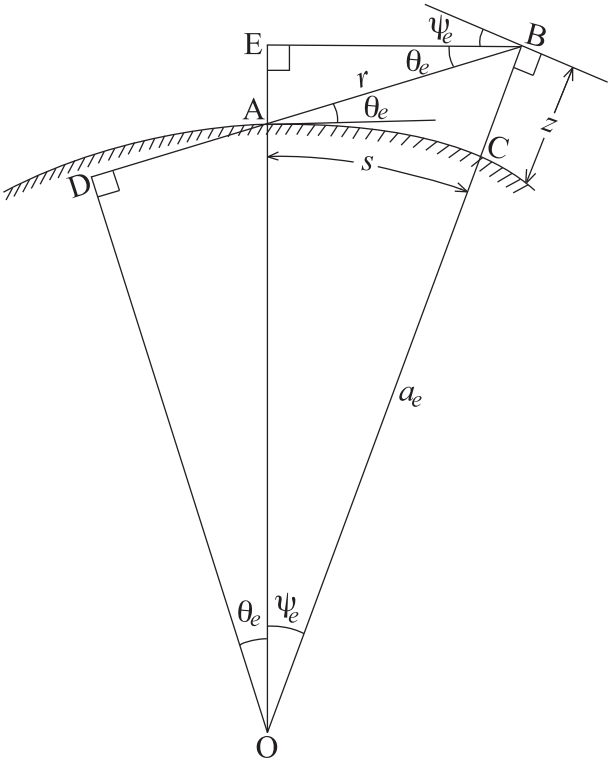

FIG. 2. Schematic drawing of radar beam (ray path) in the equivalent earth model with the transformed earth surface plotted by the hatched arc. The equivalent earth center is at point O. The radar is at point A. The radar beam is along line AB of length r. Line BC shows the beam height z at point B above the earth surface. Arc AC shows the horizontal distance s from radar to point C along the great circle.

$$R\sin\psi_e = r\sin(\pi/2 + \theta_e) = r\cos\theta_e. \tag{2.4}$$

Note that $R\sin\psi_e$ is the length of BE side of the right triangle OEB and $r\cos\theta_e$ is the length of BE side of the AEB, and this leads to (2.4) directly. From (2.3) and (2.4), we obtain $R^2\cos^2\psi_e = R^2(1 - \sin^2\psi_e) = R^2 - r^2\cos^2\theta_e = (a_e + r\sin\theta_e)^2$,

$$R\cos\psi_e = a_e + r\sin\theta_e \quad \text{and} \tag{2.5}$$

$$\tan\psi_e = r\cos\theta_e/(a_e + r\sin\theta_e). \tag{2.6}$$

Here, (2.6) recovers (A1) of Heymsfield et al. (1983), although the symbols used here are not all the same as theirs. Substituting (2.6) into (2.2) recovers (9.9) of Doviak and Zrnic (2006).

Note that s measures the arc distance of the measurement point from the radar, which is horizontal distance in the local Cartesian coordinate system centered at the radar; that is, $s = (x^2 + y^2)^{1/2}$, so using (2.3) and (2.4) z and s can be related to r and, ψ_e by

$$z = R - a_e = (a_e^2 + r^2 + 2ra_e\sin\theta_e)^{1/2} - a_e \quad \text{and} \tag{2.7}$$

$$s = a_e\psi_e = a_e\sin^{-1}[r\cos\theta_e/(a_e + z)], \tag{2.8}$$

which recover (2.28b) and (2.28c) of Doviak and Zrnic (2006). In (2.7), z is expressed as a function of (r, θ_e) and its derivative to r (for fixed θ_e) gives

$$\sin\theta = \partial z/\partial r|_{\theta_e} = (r + a_e\sin\theta_e)/R \quad \text{and} \tag{2.9}$$

$$\cos\theta = (1 - \sin^2\theta)^{1/2} = [R^2 - (r + a_e\sin\theta_e)^2]^{1/2}/R = a_e\cos\theta_e/R, \tag{2.10}$$

where (2.3) is used. Substituting (2.2) into (2.9) gives $R\sin(\theta_e + \psi_e) = r + a_e\sin\theta_e$; that is, BD = BA + AD as shown in Fig. 2. Substituting the expression of $\tan\theta$ derived from (2.9)/(2.10)—that is,

$$\tan\theta = r/(a_e\cos\theta_e) + \tan\theta_e \tag{2.11}$$

into the right-hand side of $\tan\psi_e = \tan(\theta - \theta_e) = (\tan\theta - \tan\theta_e)/(1 + \tan\theta\tan\theta_e)$ can lead to the same expression of $\tan\psi_e$ in (2.6).

In Fig. 1, the straight beams are computed by $z = z_f \equiv r\sin\theta_e$ for a flat earth model, which is degenerated from the equivalent earth model in the limit of $\theta \to \theta_e$ owing to either $a_e/a \to \infty$ or $r/a \to 0$. Subtracting $(a_e + z_f)^2 = a_e^2 + r^2\sin^2\theta_e + 2ra_e\sin\theta_e$ from $(a_e + z_e)^2 = r^2 + a_e^2 + 2ra_e\sin\theta_e$ gives

$$z_e - z_f = r^2\cos^2\theta_e/(2a_e + z_e + z_f) \approx r^2\cos^2\theta_e/(2a_e) \approx r^2/(2a_e) \quad \text{for} \quad \theta_e \le 19.5°, \tag{2.12}$$

where z_e is the curved-beam height described by (2.7) in the equivalent earth model, and $\cos\theta_e = 1 - (\pi\theta_e/180°)^2/2 + \cdots = 1 - 0.06 + \cdots \approx 1$ is used for $\theta_e \le 19.5°$. According to (2.12), the difference between the curved- and straight-beam heights for each given θ_e in Fig. 1 increases quadratically with r almost exactly in the same way for all θ_e ($\le$19.5°). Because the r coordinate is compressed relative to z coordinate and the r range is reduced successively with the increase of θ_e in Fig. 1, the above property is not visually intuitive as viewed from Fig. 1, but this property is important for understanding the numerical results presented (in Fig. 6) for the error analysis in section 4b.

3. Radial velocity equation derived with equivalent earth model

Projecting the inviscid vector momentum equation on **c** gives the following form of v_r equation:

TABLE 1. Components of $\nabla\mathbf{c}^{\mathrm{T}}$ for $\mathbf{c} = \mathbf{x}/r$ (first column) derived in (x, y, z) coordinates and (second column) expressed in (ϕ, r, θ) coordinates with $\theta = \theta_e$, where $(r^2 - z^2)/r^3 = (x^2 + y^2)/r^3 = \cos^2\theta/r$ is used.

In (x, y, z)	In (ϕ, r, θ) with $\theta = \theta_e$
$\partial c_1/\partial x\|_{y,z} = (r^2 - x^2)/r^3$	$(1 - \sin^2\phi\cos^2\theta)/r$
$\partial c_2/\partial x\|_{y,z} = -xy/r^3$	$-\sin\phi\cos\phi\cos^2\theta/r$
$\partial c_3/\partial x\|_{y,z} = -xz/r^3$	$-\sin\phi\cos\theta\sin\theta/r$
$\partial c_1/\partial y\|_{x,z} = -xy/r^3$	$-\sin\phi\cos\phi\cos^2\theta/r$
$\partial c_2/\partial y\|_{x,z} = (r^2 - y^2)/r^3$	$(1 - \cos^2\phi\cos^2\theta)/r$
$\partial c_3/\partial y\|_{x,z} = -yz/r^3$	$-\cos\phi\cos\theta\sin\theta/r$
$\partial\mathbf{c}/\partial z\|_{x,y} = (-xz, -yz, r^2 - z^2)^{\mathrm{T}}/r^3$	$(-\sin\phi\sin\theta, -\cos\phi\sin\theta, \cos\theta)^{\mathrm{T}}\cos\theta/r$

$$d_t v_r + (f\mathbf{k}\times\mathbf{v})^{\mathrm{T}}\mathbf{c} = (\mathbf{k}b - \nabla p/\rho)^{\mathrm{T}}\mathbf{c} + (\mathbf{v}^{\mathrm{T}}\nabla\mathbf{c}^{\mathrm{T}})\mathbf{v}, \tag{3.1}$$

where $d_t = \partial_t + \mathbf{v}^{\mathrm{T}}\nabla$ is the Lagrangian time differential operator, $\nabla = (\partial_x, \partial_y, \partial_z)^{\mathrm{T}}$ is the spatial gradient operator, f is the Coriolis parameter, b is the perturbation buoyancy (defined by the ratio between the perturbation and basic-state potential temperatures multiplied by the acceleration of gravity), p is perturbation pressure, and ρ is the basic-state density. The last term in (3.1) is due to the projection of the advection term $\mathbf{v}\cdot\nabla\mathbf{v}$ on $\mathbf{c}$, which gives

$$\begin{aligned}(\mathbf{v}^{\mathrm{T}}\nabla\mathbf{v})^{\mathrm{T}}\mathbf{c} &= \mathbf{c}^{\mathrm{T}}(\mathbf{v}^{\mathrm{T}}\nabla\mathbf{v}) = \mathbf{v}^{\mathrm{T}}\nabla(\mathbf{c}^{\mathrm{T}}\mathbf{v}) - (\mathbf{v}^{\mathrm{T}}\nabla\mathbf{c}^{\mathrm{T}})\mathbf{v}\\ &= \mathbf{v}^{\mathrm{T}}\nabla v_r - (\mathbf{v}^{\mathrm{T}}\nabla\mathbf{c}^{\mathrm{T}})\mathbf{v}.\end{aligned} \tag{3.2}$$

When $dn/dz \to -1/a$, $a_e/a \to \infty$ and $\theta \to \theta_e$ according to (2.2)–(2.4), so the equivalent earth model degenerates to the flat earth model with $r = |\mathbf{x}|$ and $\mathbf{c} = \mathbf{x}/r$ where $\mathbf{x} \equiv (x, y, z)^{\mathrm{T}}$. The equivalent earth model also degenerates to a flat earth model when $r/(a_e + z) = r/R \to 0$. For these degenerated cases, we have $\partial_j c_i = \partial_j(x_i/r) = \partial_j x_i/r + x_i\partial_j(1/r) = \delta_{ji}/r - x_i x_j/r^3$ or, equivalently, $\nabla\mathbf{c}^{\mathrm{T}} = \nabla(\mathbf{x}^{\mathrm{T}}/r) = \mathbf{l}/r - \mathbf{x}\mathbf{x}^{\mathrm{T}}/r$, where ∂_j denotes the jth component of ∇ and c_{i} (or x_i) is the ith component of $\mathbf{c}$ (or $\mathbf{x}$), δ_{ji} is the Kronecker delta, and $\mathbf{l}$ is the identity matrix. The last term in (3.1) is then given explicitly by

$$(\mathbf{v}^{\mathrm{T}}\nabla\mathbf{c}^{\mathrm{T}})\mathbf{v} = \mathbf{v}^{\mathrm{T}}\mathbf{v}/r - (\mathbf{v}^{\mathrm{T}}\mathbf{x}/r)(\mathbf{x}^{\mathrm{T}}\mathbf{v}/r)/r = (|\mathbf{v}|^2 - v_r^2)/r. \tag{3.3}$$

Substituting (3.3) into (3.1) gives the degenerated flat earth v_r equation. The components of $\nabla\mathbf{c}^{\mathrm{T}} = \mathbf{l}/r - \mathbf{x}\mathbf{x}^{\mathrm{T}}/r$ are listed in the first column of Table 1 and expressed in (ϕ, r, θ) coordinates (with $\theta = \theta_e$) in the second column of Table 1 for latter comparisons.

For nondegenerated cases, $\mathbf{c} \neq \mathbf{x}/r$, but $\mathbf{c}$ is still a function of (ϕ, θ) and θ is a function of (r, θ_e) as shown in (2.11), while z and $s = |(x, y)|$ are functions of (r, θ_e) as shown in (2.7) and (2.8). This implies that the last term in (3.1) can be analyzed explicitly by transforming the coordinate system from (x, y, z) to (ϕ, r, θ_e), as shown below in two steps.

The first step transforms (x, y, z) to (ϕ, s, z) or, equivalently, (x, y) to (ϕ, s) for fixed z. The related Jacobian matrix is

$$\begin{pmatrix}\partial x/\partial\phi & \partial x/\partial s\\ \partial y/\partial\phi & \partial y/\partial s\end{pmatrix} = \begin{pmatrix} s\cos\phi & \sin\phi\\ -s\sin\phi & \cos\phi\end{pmatrix}, \tag{3.4}$$

and $\partial(x, y)/\partial(\phi, s) = s$. The three column vectors of $(\nabla\mathbf{c}^{\mathrm{T}})^{\mathrm{T}}$ can be written into

$$\begin{aligned}\partial\mathbf{c}/\partial x|_{y,z} &= \partial(\mathbf{c}, y)/\partial(\phi, s)|_z/s = [(\partial\mathbf{c}/\partial\phi)\partial y/\partial s\\ &\quad - (\partial\mathbf{c}/\partial s)\partial y/\partial\phi]|_z/s,\end{aligned} \tag{3.5a}$$

$$\begin{aligned}\partial\mathbf{c}/\partial y|_{x,z} &= -\partial(\mathbf{c}, x)/\partial(\phi, s)|_z/s = [-(\partial\mathbf{c}/\partial\phi)\partial x/\partial s\\ &\quad + (\partial\mathbf{c}/\partial s)\partial x/\partial\phi]|_z/s, \quad \text{and}\end{aligned} \tag{3.5b}$$

$$\partial\mathbf{c}/\partial z|_{x,y} = \partial\mathbf{c}/\partial z|_{\phi,s}. \tag{3.5c}$$

Substituting $\mathbf{c}$ defined in (2.1) with (3.4) into (3.5) gives the component terms of $\nabla\mathbf{c}^{\mathrm{T}}$ in (ϕ, s, z) coordinates, as listed in the second column of Table 2.

The second step transforms (ϕ, s, z) to (ϕ, r, θ_e) or, equivalently, (s, z) to (r, θ_e) for fixed ϕ. The related Jacobian matrix can be derived by differentiating (2.4) and (2.3), which gives

$$\begin{aligned}&R\cos\psi_e\, ds/a_e + \sin\psi_e\, dz = \cos\theta_e\, dr - r\sin\theta_e\, d\theta_e \quad \text{and}\\ &R\, dz = (r + a_e\sin\theta_e)\, dr + r a_e\cos\theta_e\, d\theta_e\\ &\qquad = R\sin\theta\, dr + rR\cos\theta\, d\theta_e\end{aligned}$$

or, equivalently,

$$\begin{pmatrix} R\cos\psi_e/a_e & \sin\psi_e\\ 0 & 1\end{pmatrix}\begin{pmatrix} ds\\ dz\end{pmatrix} = \begin{pmatrix}\cos\theta_e & -r\sin\theta_e\\ \sin\theta & r\cos\theta\end{pmatrix}\begin{pmatrix} dr\\ d\theta_e\end{pmatrix},$$

where $R = a_e + z$, $s = a_e\psi_e$ and (2.9) and (2.10) are used. The Jacobian matrix is

$$\begin{pmatrix} \partial s/\partial r & \partial s/\partial\theta_e \\ \partial z/\partial r & \partial z/\partial\theta_e \end{pmatrix} = \begin{pmatrix} R\cos\psi_e/a_e & \sin\psi_e \\ 0 & 1 \end{pmatrix}^{-1} \begin{pmatrix} \cos\theta_e & -r\sin\theta_e \\ \sin\theta & r\cos\theta \end{pmatrix}$$
$$= \begin{pmatrix} \cos\theta_e/\cos\psi_e - \sin\theta\tan\psi_e & -r\sin\theta_e/\cos\psi_e - r\cos\theta\tan\psi_e \\ R\sin\theta/a_e & r\cos\theta_e \end{pmatrix}(a_e/R) \quad \text{and} \tag{3.6}$$

$$\partial(s,z)/\partial(r,\theta_e) = (a_e/R)[(a_e/R)(\cos\theta_e/\cos\psi_e - \sin\theta\tan\psi_e)r\cos\theta_e + r\sin\theta(\sin\theta_e/\cos\psi_e + a_e\cos\theta_e\tan\psi_e/R)]$$
$$= (a_e/R)^2[(\cos\theta_e/\cos\psi_e)r\cos\theta_e + (R/a_e)r\sin\theta(\sin\theta_e/\cos\psi_e)]$$
$$= (a_e/R)^2 r[\cos^2\theta_e + (r/a_e + \sin\theta_e)\sin\theta_e]/\cos\psi_e = (a_e r/R^2)(a_e + r\sin\theta_e)/\cos\psi_e = a_e r/R, \tag{3.7}$$

where (2.9) and (2.10) are used in the first three steps and (2.5) is used in the last step.

Applying $\cos^2\theta\partial/\partial r|_{\phi,\theta e}$ and $\cos^2\theta\partial/\partial\theta_e|_{\phi,r}$ to the two sides of (2.11) gives

$$\partial\theta/\partial r|_{\phi,\theta_e} = \cos^2\theta/(a_e\cos\theta_e) = a_e\cos\theta_e/R^2 \quad \text{and} \tag{3.8}$$

$$\partial\theta/\partial\theta_e|_{\phi,r} = (\cos\theta/\cos\theta_e)^2(r\sin\theta_e/a_e + 1)$$
$$= a_e(r\sin\theta_e + a_e)/R^2 = a_e\cos\psi_e/R, \tag{3.9}$$

where (2.10) and (2.5) are used. The results in (3.8) and (3.9) can be also obtained by applying $\cos^2\psi_e\partial/\partial r|_{\phi,\theta_e}$ and $\cos^2\psi_e\partial/\partial\theta_e|_{\phi,r}$ to the two sides of (2.6), which gives

$$\partial\psi_e/\partial r|_{\phi,\theta_e} = a_e\cos\theta_e/R^2 \quad \text{and} \tag{3.10}$$

$$\partial\psi_e/\partial\theta_e|_{\phi,r} = -r\sin\theta/R, \tag{3.11}$$

where (2.9) and (2.5) are used. Clearly, (3.10) is consistent with (3.8) because $\partial\theta/\partial r|_{\phi,\theta_e} = \partial(\theta_e + \psi_e)/\partial r|_{\phi,\theta_e} = \partial\psi_e/\partial r|_{\phi,\theta_e}$, while (3.11) is consistent with (3.9) because the two sides of (3.9) can be rewritten into

$$\partial\theta/\partial\theta_e|_{\phi,r} = \partial(\theta_e + \psi_e)/\partial\theta_e|_{\phi,r} = 1 + \partial\psi_e/\partial\theta_e|_{\phi,r} \quad \text{and}$$
$$a_e\cos\psi_e/R = a_e\cos(\theta - \theta_e)/R = a_e(\cos\theta\cos\theta_e + \sin\theta\sin\theta_e)/R = 1 - r\sin\theta/R,$$

where (2.9) and (2.10) are used in the last step.

Using (3.6)–(3.9) and (2.10), we obtain

$$\partial\theta/\partial s|_{\phi,z} = \partial(\theta,z)/\partial(s,z) = [\partial(\theta,z)/\partial(r,\theta_e)]|_\phi R/(a_e r)$$
$$= [(a_e\cos\theta_e/R^2)(a_e/R)r\cos\theta_e - (a_e\cos\psi_e/R)\sin\theta]R/(a_e r) = \cos^2\theta/a_e - \cos\psi_e\sin\theta/r. \tag{3.12}$$

Substituting (3.12) into the first six component terms in the second column of Table 2 yields their explicit expressions in (ϕ, r, θ_e) coordinates, as listed in the third column of Table 2. Substituting (3.6)–(3.9) with (2.4) and (2.10) into the last vector component term in the second column of Table 2 gives

$$\partial\mathbf{c}/\partial z|_{\phi,s} = \partial(\mathbf{c},s)/\partial(z,s)|_\phi = [(\partial\mathbf{c}/\partial r)\partial s/\partial\theta_e - (\partial\mathbf{c}/\partial\theta_e)\partial s/\partial r]|_\phi/(-a_e r/R)$$
$$= -\partial\mathbf{c}/\partial\theta|_\phi[(\partial\theta/\partial r)\partial s/\partial\theta_e - (\partial\theta/\partial\theta_e)\partial s/\partial r]|_\phi R/(a_e r)$$
$$= \partial\mathbf{c}/\partial\theta|_\phi(a_e/R)[(\cos\theta/a_e)(\sin\theta_e/\cos\psi_e + \cos\theta\tan\psi_e) + (\cos\theta_e - \sin\theta\sin\psi_e)/r]$$
$$= \partial\mathbf{c}/\partial\theta|_\phi\{\cos\theta/r + (\cos\theta/R)[\sin(\theta - \psi_e) + \cos\theta\sin\psi_e]/\cos\psi_e - a_e\sin\theta\cos\theta_e/R^2\}$$
$$= \partial\mathbf{c}/\partial\theta|_\phi(\cos\theta/r + \sin\theta\cos\theta/R - a_e\sin\theta\cos\theta_e/R^2) = \partial\mathbf{c}/\partial\theta|_\phi\cos\theta/r. \tag{3.13}$$

With $\partial\mathbf{c}/\partial\theta|_\phi = (-\sin\phi\sin\theta, -\cos\phi\sin\theta, \cos\theta)^{\mathrm{T}}$, (3.13) gives the explicit expression in the last row of the third column of Table 2.

Substituting the component terms in the third column of Table 2 into the last term in (3.1) gives

$$(\mathbf{v}^{\mathrm{T}}\nabla\mathbf{c}^{\mathrm{T}})\mathbf{v} = (|\mathbf{v}|^2 - v_r^2 + e)/r, \tag{3.14}$$

where $v_r = \mathbf{v}^{\mathrm{T}}\mathbf{c}$ but $\mathbf{c} \neq \mathbf{x}/r$ unlike in (3.3), $e = (e_2 w_{vt} - e_1 v_{ht})v_{hr}$, e_1 and e_2 are given in the caption of Table 2, $v_{ht} = u\cos\phi - v\sin\phi$ is the tangential component of

TABLE 2. Components of $\nabla \mathbf{c}^{\mathrm{T}}$ (first column) formulated in (x, y, z) coordinates, and expressed in (second column) (ϕ, s, z) coordinates and (third column) (ϕ, r, θ_e) coordinates, where $e_1 \equiv 1 - r\cos\theta/s$ and $e_2 \equiv (1 - \cos\psi_e)\sin\theta + r\cos^2\theta/a_e$.

In (x, y, z)	In (ϕ, s, z)	In (ϕ, r, θ_e)
$\partial c_1/\partial x\vert_{y,z}$	$\cos^2\phi\cos\theta/s - \sin^2\phi\sin\theta\partial\theta/\partial s\vert_{\phi,z}$	$(1 - \sin^2\phi\cos^2\theta)/r - (e_1\cos^2\phi + e_2\sin^2\phi\sin\theta)/r$
$\partial c_2/\partial x\vert_{y,z}$	$-\sin\phi\cos\phi(\cos\theta/s + \sin\theta\partial\theta/\partial s\vert_{\phi,z})$	$-\sin\phi\cos\phi\cos^2\theta/r + (e_1 - e_2\sin\theta)\sin\phi\cos\phi/r$
$\partial c_3/\partial x\vert_{y,z}$	$\sin\phi\cos\theta\partial\theta/\partial s\vert_{\phi,z}$	$-\sin\phi\cos\theta\sin\theta/r + e_2\sin\phi\cos\theta/r$
$\partial c_1/\partial y\vert_{x,z}$	$-\cos\phi\sin\phi(\cos\theta/s + \sin\theta\partial\theta/\partial s\vert_{\phi,z})$	$-\sin\phi\cos\phi\cos^2\theta/r + (e_1 - e_2\sin\theta)\sin\phi\cos\phi/r$
$\partial c_2/\partial y\vert_{x,z}$	$\sin^2\phi\cos\theta/s - \cos^2\phi\sin\theta\partial\theta/\partial s\vert_{\phi,z}$	$(1 - \cos^2\phi\cos^2\theta)/r - (e_1\sin^2\phi + e_2\cos^2\phi\sin\theta)/r$
$\partial c_3/\partial y\vert_{x,z}$	$\cos\phi\cos\theta\partial\theta/\partial s\vert_{\phi,z}$	$-\cos\phi\cos\theta\sin\theta/r + e_2\cos\phi\cos\theta/r$
$\partial \mathbf{c}/\partial z\vert_{x,y}$	$\partial \mathbf{c}/\partial z\vert_{\phi,s}$	$(-\sin\phi\sin\theta, -\cos\phi\sin\theta, \cos\theta)^{\mathrm{T}}\cos\theta/r$

$\mathbf{v}_h \equiv (u, v)$ perpendicular to the beam in the horizontal plane, $v_{hr} = u\sin\phi + v\cos\phi$ is the radial component of $\mathbf{v}_h$ along the beam azimuth in the horizontal plane, and $w_{vt} = w\cos\theta - v_{hr}\sin\theta$ is the vertical tangential component of $\mathbf{v}$ perpendicular to the beam in the vertical plane. Substituting (3.14) into (3.1) gives the v_r equation derived with the equivalent earth model in the following form:

$$d_t v_r + (f\mathbf{k}\times\mathbf{v})^{\mathrm{T}}\mathbf{c} = (\mathbf{k}b - \nabla p/\rho)^{\mathrm{T}}\mathbf{c} + (|\mathbf{v}|^2 - v_r^2 + e)/r. \tag{3.15}$$

When the effects of atmospheric refraction and earth curvature are neglected, (3.15) degenerates to the flat earth v_r equation in which r, $\mathbf{c}$, $v_r = \mathbf{v}^{\mathrm{T}}\mathbf{c}$, and e reduce to $|\mathbf{x}|$, $\mathbf{x}/r$, $v_r = \mathbf{v}^{\mathrm{T}}\mathbf{x}/r$, and 0, respectively.

4. Truncated radial velocity equation and error analyses

a. *Truncated radial velocity equation and smallness of truncation error*

For operational WSR-88D scans, $0.5°(\pi/180°) = \pi/360 \le \theta_e < 20°(\pi/180°) = \pi/9$ and $r < r_{\max} = 300$ km, so $z \ll r \ll a_e$ ($\approx 4a/3 \approx 8500$ km) $< R$, a_e/R is very close to 1, and $\psi_e \approx \sin\psi_e = r\cos\theta_e/R < r/R < r/a_e < 0.035r/r_{\max}$ according to (2.4). Therefore, e_1 and e_2 are small positive parameters bounded by

$$e_1 = 1 - r\cos\theta/s = 1 - \sin\psi_e/\psi_e < \psi_e^2/3! < (r/r_{\max})^2 2\times 10^{-4} \quad \text{and} \tag{4.1a}$$

$$e_2 = (1 - \cos\psi_e)\sin\theta + r\cos^2\theta/a_e < (\psi_e^2/2!)\sin\theta + r/a_e < (r/r_{\max})3.5\times 10^{-2}, \tag{4.1b}$$

where (2.4) and (2.10) are used. Neglecting e_1 and e_2, the component terms in the third column of Table 2 reduce formally to those in the second column of Table 1 but $\mathbf{c} \neq \mathbf{x}/r$, and (3.15) is truncated into

$$d_t v_r + (f\mathbf{k}\times\mathbf{v})^{\mathrm{T}}\mathbf{c} = (\mathbf{k}b - \nabla p/\rho)^{\mathrm{T}}\mathbf{c} + (|\mathbf{v}|^2 - v_r^2)/r. \tag{4.2}$$

By substituting (4.1a) and (4.1b) into $e = (e_2 w_{vt} - e_1 v_{ht})v_{hr}$ defined in (3.14), we can estimate the truncation error relative to $|\mathbf{v}|^2$ as follows:

$$|e|/|\mathbf{v}|^2 = |e_2 w_{vt} v_{hr} - e_1 v_{ht} v_{hr}|/|\mathbf{v}|^2 \approx e_2 |w_{vt} v_{hr}|/|\mathbf{v}|^2 < e_2 < (r/r_{\max})3.5\%. \tag{4.3}$$

Thus, the truncated part in the last term of (3.14) is much smaller than the major part—that is, $|\mathbf{v}|^2$ in the last term.

The upper bound of $|e|/|\mathbf{v}|^2$ estimated in (4.3) can be verified numerically by computing $e/|\mathbf{v}|^2$ at each beam height of the radar scan in a vertical column within a convective storm. Vertical profiles of (u, v, w, w_T) are extracted from the main updraft area within the simulated Oklahoma squall line (valid at 2200 UTC 2 June 2004) produced by the control run in Xu et al. (2010). The extracted vertical profiles are plotted in Fig. 3. By

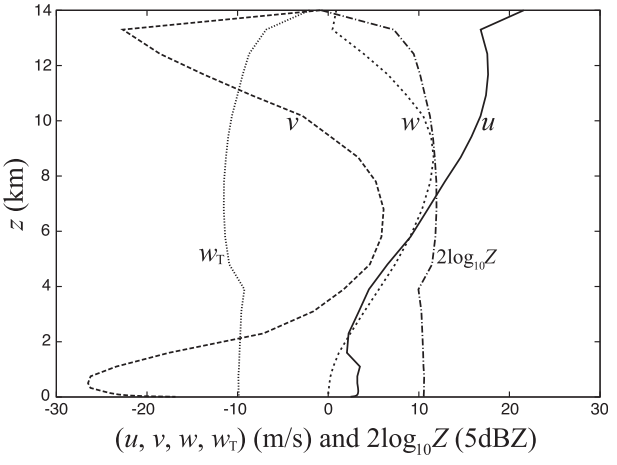

FIG. 3. Vertical profiles of (u, v, w, w_T) and $2\log_{10}Z$ (plotted in units of 5 dBZ) extracted from the main updraft area within the simulated Oklahoma squall line (valid at 2200 UTC 2 Jun 2004) produced by the control run in Xu et al. (2010), where Z is the reflectivity factor ($\mathrm{mm}^6\,\mathrm{m}^{-3}$) [see section 4.4.5 of Doviak and Zrnic (2006)].

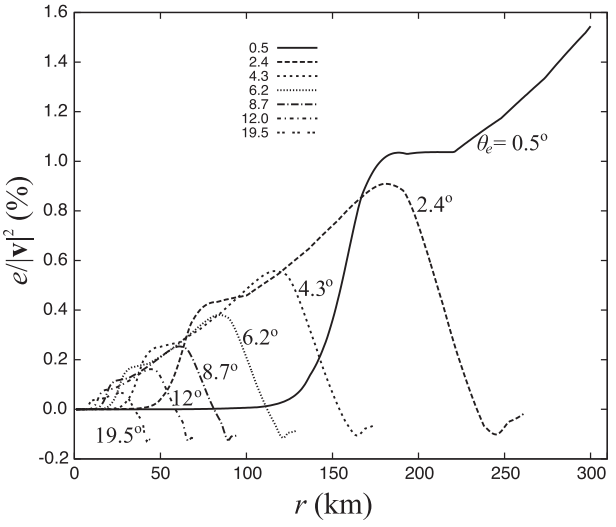

FIG. 4. Relative truncation error $e/|\mathbf{v}|^2$ (%), defined in (4.3), as a function of r for each θ_e selected in Fig. 1.

assuming that this vertical column is located to the east ($\phi = 90°$) of the radar at variable distance s (so that r is also variable), $e/|\mathbf{v}|^2$ is computed and plotted as a function of r in Fig. 4 for each θ_e selected in Fig. 1. As shown in Fig. 4, $|e|/|\mathbf{v}|^2$ is bounded at least by $(r/r_{\max}) \times 1.8\%$ regardless of the variations of $e/|\mathbf{v}|^2$ with (r, θ_e). This main feature remains the same for different settings of ϕ and different vertical profiles of $\mathbf{v}$ (not shown), and the numerically estimated upper bound verifies and tightens the analytically estimated upper bound of $|e|/|\mathbf{v}|^2$ in (4.3). Since $|e|/|\mathbf{v}|^2$ is indeed very small, the truncated v_r equation in (4.2) has virtually the same accuracy as the full v_r equation in (3.15).

b. Error of degenerated flat earth radial velocity equation

The truncated v_r equation in (4.2) has the same concise form as the degenerated v_r equation but the latter contains significant errors owing to the flat earth approximation. When (4.2) is used as a dynamic constraint for radar wind analysis or assimilation, v_r contained in the first and last terms should match the processed radial velocity observations, denoted by v_r^{po}, that passed proper data quality control, including a bias correction step after dealiasing [see section 3.1 of Xu et al. (2010)] to produce $v_r^{\text{po}} = v_r^{\text{ob}} - w_T^e \mathbf{k}^{\text{T}}\mathbf{c}$, where w_T^e (<0) is the terminal velocity estimated from the observed reflectivity [see (5) of Xu et al. (2010)]. The flat earth model can have a significant error in the radar-beam height assigned to v_r^{ob} and therefore cause a displaced-sampling error in v_r^{ob} especially if the true v_r changes significantly from the assigned height to the true height of v_r^{ob}. This can cause a large error in the v_r equation as evaluated below.

First, we compute $v_r^{\text{po}} = v_r^{\text{ob}} - w_T^e \mathbf{k}^{\text{T}}\mathbf{c}$ as a function of (r, θ_e) for given ϕ from the vertical profiles of (u, v, w, w_T) in Fig. 3 by using the equivalent earth model (with $a/a_e = 3/4$) and denote the result by v_r^{poe}. We then compute $v_r^{\text{po}} = v_r^{\text{ob}} - w_T^e \mathbf{k}^{\text{T}}\mathbf{x}/r$ also as a function of (r, θ_e) but using the flat earth model (with $a/a_e = 0$) and denote the result by v_r^{pof}. Considering the effect of finite beamwidth, v_r^{poe} is computed as a function of (θ_e, r) by

$$v_r^{\text{poe}}(\theta_e, r) = \int G(\theta')[Z(\mathbf{v} + w_T\mathbf{k})^{\text{T}}\mathbf{c}]\, d\theta' \Big/ \int G(\theta') Z\, d\theta' - w_T^e \mathbf{k}^{\text{T}}\mathbf{c}, \tag{4.4a}$$

where $\int(\cdot)\, d\theta'$ denotes the integral of $(\cdot)$ computed by the summation of $(\cdot)$ over $-\Delta\theta/2 \le \theta' \le \Delta\theta/2$ with a sufficiently high resolution, $\Delta\theta = 1°$ is the beamwidth in elevation angle, and $G(\theta') = \exp[-(4\ln 4)(\theta'/\Delta\theta)^2]$ is the two-way power-gain distribution within the radar beam [(5.40), (5.48), and (5.53) of Doviak and Zrnic (2006)], and Z is the reflectivity factor [see section 4.4.5 of Doviak and Zrnic (2006)]. Here, for the integral term in (4.4a), Z, $\mathbf{v} = (u, v, w)^{\text{T}}$, and w_T are functions of z given in Fig. 3, with z computed as a function of $(\theta_e + \theta', r)$ by setting θ_e to $\theta_e + \theta'$ in (2.7), and $\mathbf{c}$ is a function of (θ, ϕ) defined in (2.1), with θ computed as a function of $(\theta_e + \theta', r)$ by setting θ_e to $\theta_e + \theta'$ in $\tan^{-1}$[(2.11)]. For the last term in (4.4a), z and θ are computed just as functions of (θ_e, r) from (2.7) and $\tan^{-1}$[(2.11)], respectively. Similarly, v_r^{pof} is computed as a function of (θ_e, r) by

$$v_r^{\text{pof}}(\theta_e, r) = \int G(\theta')[Z(\mathbf{v} + w_T\mathbf{k})^{\text{T}}\mathbf{x}/r]\, d\theta' \Big/ \int G(\theta') Z\, d\theta' - w_T^e \mathbf{k}^{\text{T}}\mathbf{x}/r, \tag{4.4b}$$

where Z, $\mathbf{v} = (u, v, w)^{\text{T}}$, and w_T are still given by the vertical profiles in Fig. 3, but z is computed as a function of $(\theta_e + \theta', r)$ by $z = r\sin(\theta_e + \theta')$ and $\mathbf{x}/r$ is computed as a function of $(\theta_e + \theta', \phi)$ by $\mathbf{x}/r = [\cos(\theta_e + \theta')\sin\phi, \cos(\theta_e + \theta')\cos\phi, \sin(\theta_e + \theta')]^{\text{T}}$ for the integral term in (4.4b). For the last term in (4.4b), z and θ are computed

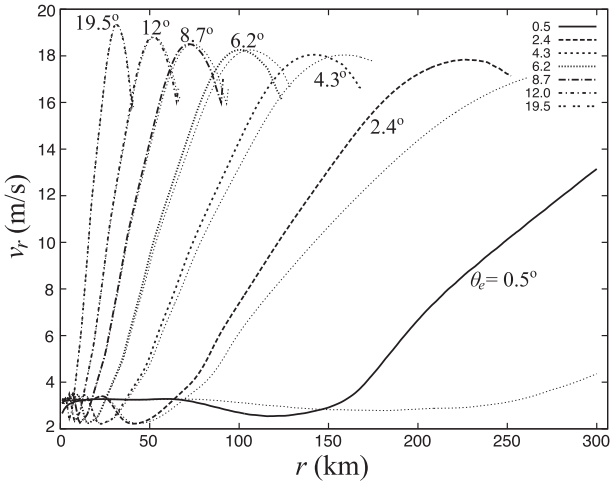

FIG. 5. Radial velocity observation $v_r^{\mathrm{poe}}(\theta_e, r)$, simulated by using (4.4a) with the equivalent earth model, plotted by each dark curve as a function of r for each θ_e selected in Fig. 1. The thin dotted curve associated with each dark curve is the radial velocity observation $v_r^{\mathrm{pof}}(\theta_e, r)$ simulated by using (4.4b) with the flat earth model.

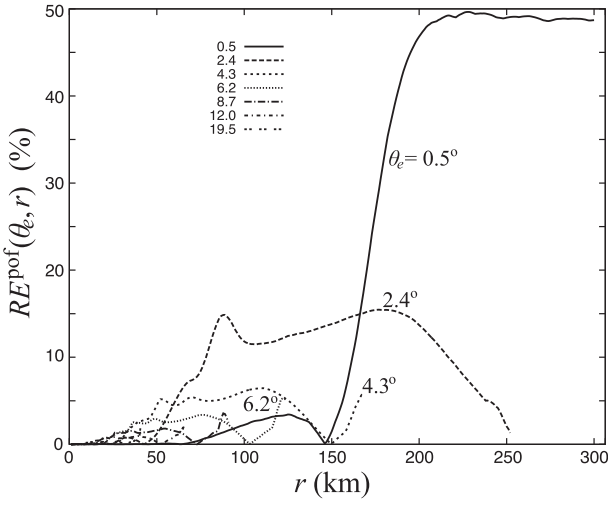

FIG. 6. Relative error estimated in (4.5) for $v_r^{\mathrm{pof}}(\theta_e, r)$ [$\mathrm{RE}^{\mathrm{pof}}(\theta_e, r)$] (%), plotted by each dark curve as a function of r for each θ_e selected in Fig. 1.

just as functions of (θ_e, r) by $z = r\sin\theta_e$ and $\mathbf{x}/r = (\cos\theta_e \sin\phi, \cos\theta_e \cos\phi, \sin\theta_e)^{\mathrm{T}}$, respectively.

The computed v_r^{poe} (v_r^{pof}) with $w_T^e = w_T$ is plotted by a thick (thin) curve in Fig. 5 as a function of r for each θ_e (selected in Fig. 1) with $\phi = 90°$. Since the height assignment error for v_r^{poe} is much smaller than that for v_r^{pof} (as will be seen later), the error in v_r^{pof} relative to $|\mathbf{v}|$ can be denoted and estimated by

$$\mathrm{RE}^{\mathrm{pof}}(\theta_e, r) = |v_r^{\mathrm{pof}}(\theta_e, r) - v_r^{\mathrm{poe}}(\theta_e, r)|/|\mathbf{v}(\theta_e, r)|, \quad (4.5)$$

where $\mathbf{v}(\theta_e, r) = \mathbf{v}[z(\theta_e, r)]$ is taken from the vertical profiles in Fig. 3 at the beam height—that is, z computed from (2.7) for given (θ_e, r). The estimated $\mathrm{RE}^{\mathrm{pof}}(\theta_e, r)$ is plotted in Fig. 6. As shown, $E^{\mathrm{pof}}(\theta_e, r)$ becomes larger than 10% as r exceeds 75 km on $\theta_e = 2.4°$, and becomes larger than 25% as r exceeds 180 km on the lowest tilt ($\theta_e = 0.5°$). According to (4.4) and (4.5), E^{pof} is essentially the difference between $\mathbf{v}^{\mathrm{T}}\mathbf{c}$ at $z = z_e(\theta_e, r)$ and $\mathbf{v}^{\mathrm{T}}\mathbf{x}/r$ at $z = z_f(\theta_e, r)$ normalized by $|\mathbf{v}|$ at $z = z_e(\theta_e, r)$, where $z_e(\theta_e, r)$ and $z_f(\theta_e, r)$ are defined in (2.12) and plotted as paired functions of r for each θ_e in Fig. 1. Since $\mathbf{c}$ and $\mathbf{x}$ are smooth functions of (θ_e, r), the rapid variations of E^{pof} with r are caused mainly by the rapid differential variations of $\mathbf{v}$ between $z_e(\theta_e, r)$ and $z_f(\theta_e, r)$, while the upper bound of these variations are largely controlled by $z_e - z_f \approx r^2/(2a_e)$, independent of θ_e as shown in (2.12). This explains the gross pattern of the envelope (not shown but can be perceived) of all the $\mathrm{RE}^{\mathrm{pof}}(r)$ curves plotted for the different θ_e in Fig. 6. This feature and the qualitative aspect of the above results remain the same for different settings of ϕ and different selections of vertical profile of $\mathbf{v}$ (not shown). Note that v_r is linear in $d_t v_r$, so the relative error caused in the first term of (4.2) owing to the use of the flat earth model can be estimated roughly by $\mathrm{RE}^{\mathrm{pof}}(\theta_e, r)$. On the other hand, since v_r is quadratic in $(|\mathbf{v}|^2 - v_r^2)/r$, the relative error caused in the last term of (4.2) by the flat earth model should be estimated by the square of $\mathrm{RE}^{\mathrm{pof}}(\theta_e, r)$. Because $[\mathrm{RE}^{\mathrm{pof}}(\theta_e, r)]^2 < \mathrm{RE}^{\mathrm{pof}}(\theta_e, r)$ according to the results in Fig. 6 and $(|\mathbf{v}|^2 - v_r^2)/r$ becomes a small term in (4.2) as r increases to 80 km and beyond, the error of the flat earth v_r equation is mainly in the first term of (4.2), and this error can be estimated by $\mathrm{RE}^{\mathrm{pof}}(\theta_e, r)$.

c. *Error of truncated equivalent earth radial velocity equation*

As reviewed in section 2, the equivalent earth model assumes that the vertical gradient of refractivity index is constant in the lower troposphere, and this gradient is commonly set to the typical value of $dn/dz = -1/(4a)$. In the real atmosphere, however, dn/dz is not constant and its value can fluctuate over a wide range around the above typical value in the lower troposphere ($z \le 2$ km). Occasionally, adn/dz can decrease drastically below -1 within a temperature inversion and/or strong moisture gradient layer in the lower troposphere to cause the radar beam on the lowest tilt ($\theta_e = 0.5°$) to bend back toward Earth's surface and therefore produce ground clutter and near-zero values in radial velocity observations. Since ground clutter and associated near-zero velocity must be removed through data quality control, this type of rarely occurring abnormal situation is not considered here. In normal situations, the equivalent earth model can be used to estimate the beam height (Gao et al.

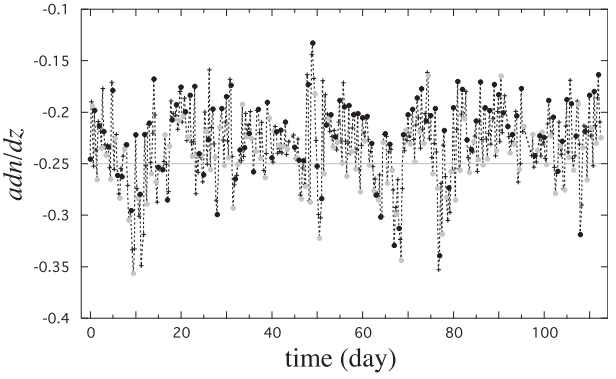

FIG. 7. Time series of adn/dz (averaged over the depth of $0 \le z \le 2$ km) computed from the vertical profiles of temperature and specific humidity collected every 6 h over the period from 0000 UTC 22 Nov 2012 to 1200 UTC 14 Mar 2013 at the operational sounding station LMN at Lamont, Oklahoma, within the Southern Great Plains (SGP) site established by the Department of Energy's Atmospheric Radiation Measurement Program (ARM). The gray (black) dots plot the values computed from the early morning (late afternoon) soundings at 0600 (1800) LT, while the plus signs plot the values computed from the soundings at the local noon and midnight.

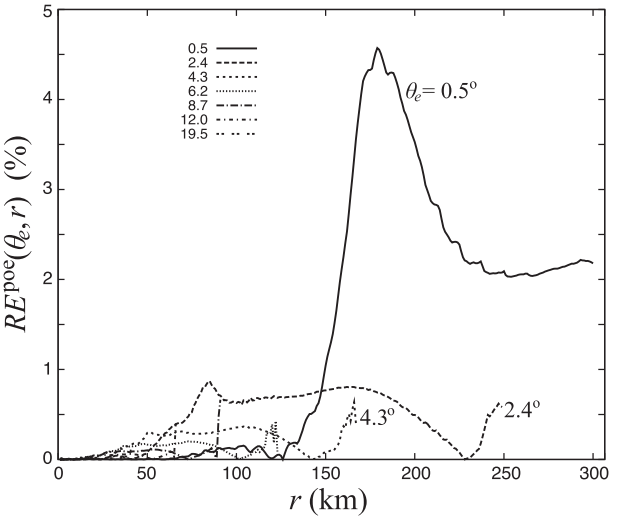

FIG. 8. Relative error estimated by (4.6) for $v_r^{\mathrm{poe}}(\theta_e, r)$ [$\mathrm{RE}^{\mathrm{poe}}(\theta_e, r)$] (%), plotted by each dark curve as a function of r for each θ_e selected in Fig. 1.

2006, 2008), but setting $adn/dz = -1/4$ can cause an error in the estimated beam height if this commonly used value of $adn/dz = -1/4$ is different from the true value of adn/dz in the lower troposphere. This can cause a small error in the v_r equation as evaluated below.

To evaluate the aforementioned error, vertically averaged values of adn/dz over the depth of $0 \le z \le 2$ km are computed from the vertical profiles of temperature and specific humidity collected over the period from 0000 UTC 22 November 2012 to 1200 UTC 14 March 2013 at the operational sounding station LMN at Lamont, Oklahoma. As shown in Fig. 7, the values computed from the early morning soundings at 0600 LT (plotted by the gray dots) are generally more negative than those computed from the latter afternoon soundings at 1800 LT (plotted by the black dots), and this is simply because the vertical stratifications of temperature and specific humidity in the lower troposphere are generally stronger in the early morning than in the latter afternoon. From the time series in Fig. 7, we can also see that the vertically averaged value of adn/dz fluctuates between -0.357 and -0.133, the time mean is -0.233 and the standard deviation is 0.036. These results indicate that the error for the commonly used value of $adn/dz = -0.25$ is time dependent and fluctuates between 0.107 and -0.107, while the bias is -0.017 and the RMS error is 0.040. The RMS error for $a/a_e = 1 + adn/dz$ is thus also 0.04, which is much smaller than the dramatic change of value in a/a_e (from 3/4 to 0) caused by using the flat earth model. Therefore, the error in v_r^{poe} caused by fixing $adn/dz = -0.25$ should be much smaller than the error in v_r^{pof} caused by the flat earth model. To verify this, we set $adn/dz = -0.25 \pm 0.04$ to compute $v_r^{\mathrm{poe}}(\theta_e, r)$ from (4.4a) with $w_T^e = w_T$, denote the two computed values by $v_r^{\mathrm{poe}+}(\theta_e, r)$ and $v_r^{\mathrm{poe}-}(\theta_e, r)$, respectively, and then use

$$\mathrm{RE}^{\mathrm{poe}}(\theta_e, r) = 0.5|v_r^{\mathrm{poe}+}(\theta_e, r) - v_r^{\mathrm{poe}-}(\theta_e, r)|/|\mathbf{v}(\theta_e, r)| \tag{4.6}$$

to estimate the RMS error in v_r^{poe} (caused by using $adn/dz = -0.25$) relative to $|\mathbf{v}|$. As shown in Fig. 8, $\mathrm{RE}^{\mathrm{poe}}(\theta_e, r)$ increases in general as θ_e becomes small and r becomes large, but it does not exceed 5% even on the lowest tilt ($\theta_e = 0.5°$). The qualitative aspect of the above results remains the same for different settings of ϕ and different selections of vertical profile of $\mathbf{v}$ (not shown). Again, for the same reason as explained for $\mathrm{RE}^{\mathrm{pof}}(\theta_e, r)$ in section 4b, the relative RMS errors caused by setting $adn/dz = -0.25$ can be estimated by $\mathrm{RE}^{\mathrm{poe}}(\theta_e, r)$ and $[\mathrm{RE}^{\mathrm{poe}}(\theta_e, r)]^2$ for the first and last terms in (4.2), respectively, while the relative RMS error caused by setting $adn/dz = -0.25$ for the v_r equation in (4.2) is mainly in the first term and thus also less than 5%.

So far, by setting $w_T^e = w_T$ in this and previous subsections, we have not yet considered possible errors in the estimated terminal velocity. In fact, even if $w_T^e = w_T$, the estimated terminal velocity is still not exactly accurate because of not including the effect of finite beamwidth, although the error is very small (within $\pm 0.18\ \mathrm{m\ s^{-1}}$ and within $\pm 0.7\%$ of $|\mathbf{v}|$). The accurate estimate should satisfy $w_T^e \mathbf{k}^{\mathrm{T}}\mathbf{c} = \int G(\theta') w_T \mathbf{k}^{\mathrm{T}}\mathbf{c}\, d\theta' / \int G(\theta')\, d\theta'$ exactly.

Nevertheless, since w_T^e is usually estimated empirically from the observed reflectivity, the error can be as large as ±20% of the true $|w_T|$ (or even ±50% of the true $|w_T|$ especially in the graupel or hail region aloft where the air density is low within a severe storm), but its resulting errors in v_r^{poe} and v_r^{pof} are within ±0.8 (or ±2.0) m s^{-1} and within ±12% (or ±30%) of $|\mathbf{v}|$ for the cases considered above, according to our computations (omitted here). These errors are independent of the displaced-sampling errors estimated above for v_r^{pof} and v_r^{poe}, and they also cause errors independently in the v_r equations.

5. Conclusions

In this paper, the prognostic equation for radial velocity is derived using the equivalent earth model to include the effects of atmospheric refraction and earth curvature on radar-beam height and slope angle. The derived equation contains a high-order small term that can be truncated without degrading the accuracy achieved (and also limited) owing to the use of the equivalent earth model. In particular, as estimated analytically [see (4.3)], the upper bound of the truncated term [that is, e/r in (3.25)] is only a few percent of $|\mathbf{v}|^2/r_{\max}$, where $r_{\max}$ = 300 km is the maximum radial range of the operational radar scans. This upper bound is verified numerically and tightened [by about 50%, as shown in Fig. 4 versus (4.3)]. The truncated radial velocity equation is shown to be much more accurate than its counterpart radial velocity equation (Xu et al. 2001b) derived without considering the effects of atmospheric refraction and earth curvature. In particular, using the equivalent earth model with the vertical gradient of refractivity index set to the commonly used typical value ($dn/dz = -0.25/a$) in the lower troposphere can cause only a small relative RMS error (<5%, as shown in Fig. 8) in the truncated radial velocity equation if the true vertical gradient of refractivity index is not too different from the typical value in the lower troposphere (see Fig. 7), but the relative error caused by neglecting the effects of atmospheric refraction and earth curvature in the counterpart radial velocity equation can become larger than 25% as the range distance exceeds 180 km on the lowest tilt (see Fig. 6).

The truncated equation has the same concise form as that in Xu et al. (2001b) and can be used as a dynamic constraint for radar wind analysis in the same way as in Xu et al. (2001b), but the effects of atmospheric refraction and earth curvature are no longer neglected so operational WSR-88D radial velocity observations can be used to full radial ranges (up to 300 km). The radial velocity equation in the 3.5DVar included the above effects but neglected the perturbation pressure and buoyancy terms [see (15) of Xu et al. (2010)], so the radial velocity equation derived in this paper can be used to upgrade the dynamic constraint in the 3.5DVar for radar data assimilation. This is under current research.

Acknowledgments. The authors are thankful to Guoqing Ge of the University of Oklahoma (OU), Richard Doviak of NSSL, and anonymous reviewers for their comments and suggestions that improved the paper and to Kang Nai and Yuan Jiang of OU for their help in producing Figs. 2 and 7. The research was supported by ONR Grant N000141010778 to OU. Funding was also provided by NOAA/OAR under NOAA-OU Cooperative Agreement NA17RJ1227, U.S. Department of Commerce.

REFERENCES

Doviak, R. J., and D. S. Zrnic, 2006: *Doppler Radar and Weather Observations.* 2nd ed. Dover Publications, 562 pp.

Gao, J., K. Brewster, and M. Xue, 2006: A comparison of the radar ray path equations and approximations for use in radar data assimilation. *Adv. Atmos. Sci.,* **23,** 190–198.

——, ——, and ——, 2008: Variation of radio refractivity with respect to moisture and temperature and influence on radar ray path. *Adv. Atmos. Sci.,* **25,** 1098–1106.

Ge, G., J. Gao, K. Brewster, and M. Xue, 2010: Impacts of beam broadening and earth curvature on storm-scale 3D variational data assimilation of radial velocity with two Doppler radars. *J. Atmos. Oceanic Technol.,* **27,** 617–636.

Gu, W., H. Gu, and Q. Xu, 2001: Impact of single-Doppler radar observations on numerical prediction of 7 May 1995 Oklahoma squall line. Preprints, *Fifth Symp. on Integrated Observing Systems,* Albuquerque, NM, Amer. Meteor. Soc., 139–142. [Available online at https://ams.confex.com/ams/annual2001/techprogram/paper_17251.htm.]

Heymsfield, G. M., K. K. Ghosh, and L. C. Chen, 1983: An interactive system for compositing digital radar and satellite data. *J. Climate Appl. Meteor.,* **22,** 705–713.

Qiu, C., and Q. Xu, 1996: Least-square retrieval of microburst winds from single-Doppler radar data. *Mon. Wea. Rev.,* **124,** 1132–1144.

Xu, Q., 2011: Measuring information content from observations for data assimilation: Spectral formulations and their implications to observational data compression. *Tellus,* **63A,** 793–804.

——, and C. Qiu, 1995: Adjoint-method retrievals of low-altitude wind fields from single-Doppler reflectivity and radial-wind data. *J. Atmos. Oceanic Technol.,* **12,** 1111–1119.

——, and L. Wei, 2011: Measuring information content from observations for data assimilation: Utilities of spectral formulations for radar data compression. *Tellus,* **63A,** 1014–1027.

——, C. Qiu, and J. Yu, 1994: Adjoint-method retrievals of low-altitude wind fields from single-Doppler wind data. *J. Atmos. Oceanic Technol.,* **11,** 579–585.

——, ——, H. Gu, and J. Yu, 1995: Simple adjoint retrievals of microburst winds from single-Doppler radar data. *Mon. Wea. Rev.,* **123,** 1822–1833.

——, H. Gu, and C. J. Qiu, 2001a: Simple adjoint retrievals of wet-microburst winds and gust-front winds from single-Doppler radar data. *J. Appl. Meteor.,* **40,** 1485–1499.

——, ——, and S. Yang, 2001b: Simple adjoint method for three-dimensional wind retrievals from single-Doppler radar. *Quart. J. Roy. Meteor. Soc.,* **127,** 1053–1067.

——, L. Wei, W. Gu, J. Gong, and Q. Zhao, 2010: A 3.5-dimensional variational method for Doppler radar data assimilation and its application to phased-array radar observations. *Adv. Meteor.,* **2010,** 797265, doi:10.1155/2010/797265.

Zhao, Q., J. Cook, Q. Xu, and P. Harasti, 2006: Using radar wind observations to improve mesoscale numerical weather prediction. *Wea. Forecasting,* **21,** 502–522.

——, ——, ——, and ——, 2008: Improving short-term storm predictions by assimilating both radar radial-wind and reflectivity observations. *Wea. Forecasting,* **23,** 373–391.